Eur. Phys. J. Special Topics **143**, 109–116 (2007)

DOI: 10.1140/epjst/e2007-00078-x

THE EUROPEAN PHYSICAL JOURNAL SPECIAL TOPICS

Measures of complexity for 3D image analysis of trabecular bone

N. Marwan[1], P. Saparin[2], and J. Kurths[1]

[1] Nonlinear Dynamics Group, Institute of Physics, University of Potsdam, 14415 Potsdam, Germany
[2] Department of Biomaterials, Max-Planck-Institute of Colloids and Interfaces, 14424 Potsdam-Golm, Germany

Abstract. Based on fractal properties and spatial auto-correlation, the measures of complexity lacunarity, Moran's I and Geary's C index are defined for 3D image analysis. Their abilities to investigate translational invariance, characteristic length scales, spatial correlation and shapes of 3D micro-structures are demonstrated on proto-typical examples. Finally, using these measures of complexity, 3D images of trabecular bone are analysed. The main findings are that the complexity of the trabecular structure decreases and the plate-like shapes of the trabeculae change to mainly rod-like shapes during bone loss. These results and the proposed measures could have a great impact for medicine and for space exploration.

1 Introduction

In the last years, it has been shown that the structure of trabecular bone is very important for the stability and strength of bone [4,7,9,10,12,17,18]. Together with loss of bone mass, structural changes in the trabecular bone occur during the development of osteopenia and osteoporosis as well as under microgravity conditions [23], and can lead to an increased risk of bone fracture. Therefore, it is important not only to determine the bone mineral density but also the changes of the bone micro-architecture. Recent developments in computer tomography (CT) imaging allows for the study of high-resolution 3D images of bone. In particular, due to the recent introduction of μCT devices, images of the bone micro-architecture with resolution up to 20 μm are available.

The bone mineral density (BMD) is the standard predictor for the bone state, strength and fracture risk. Recent studies investigating trabecular bone structure have used different approaches to describe the changes in the complex micro-architecture in order to find additional descriptors for the bone state. The gold standard for the description of the trabecular bone structure is histomorphometry [13]. By using histomorphometry, good correlation between bone strength and, e. g., the mean trabecular plate separation was found [21]. Other approaches use techniques based on nonlinear data analysis, like the study of fractal properties [5,16] or symbolic encoding [19,20]. They have found clear relations between the complexity of the trabecular bone and the osteoporotic stage. Several attempts in numerical modelling of the trabecular bone and applications of finite element analysis also confirmed the importance of the trabecular bone structure for the bone strength [8,15,22].

Here we present two approaches of measures of complexity for the investigation of 3D structures, in particular 3D μCT images of trabecular bone. The first approach is based on fractal properties and uses a measure called *lacunarity*. The second approach studies spatial correlations and uses the two measures *Moran's I index* and *Geary's C index*, which actually came from the analysis of population dynamics.

These measures of complexity are applied on μCT images of biopsies of human proximal tibia.

2 Lacunarity

Lacunarity is a measure introduced to distinguish between fractal structures of different appearance, but same fractal dimension. The appearance of fractal patterns can be rather different even for the same fractal dimension. Some patterns, e. g., show larger gaps than others (cp. two Sierpinsky carpets with the same dimension but of differently scattered eliminated squares in Fig. 1). Therefore, Mandelbrot has introduced an additional term which describes such feature of "more-or-less-gaps": the *lacunarity* [11]. Patterns with larger gaps have a higher lacunarity than those with smaller gaps. In a more general sense, the higher the lacunarity of a pattern, the less translational invariant it is.

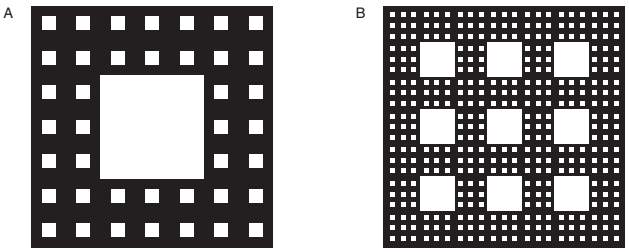

Fig. 1. (A) and (B) different Sierpinsky carpets with the same fractal dimension $D_f \approx 1.8957$ but of differently scattered eliminated squares.

Such a property is also of interest in the study of the micro-architecture of trabecular bone. Different osteoporotic stages cause differently deteriorated trabeculae, i.e. larger gaps and holes for a higher degree of osteoporosis.

In [5], the lacunarity was already applied to 2D CT images. However, this investigation was of more exemplary nature; they have not studied a large set of real bone images in regard of various osteoporotic stages.

For an additional view on 3D images of bone biopsies it may be useful, to analyze their level of translational invariance. Moreover, with the analysis of the lacunarity as a function of the box size, typical scales in the objects can be determined.

The definition of the lacunarity has slightly changed over the time. However, all definitions are based on the fluctuations of the mass distribution within a box sliding over the entire object (non-overlapping boxes). The number of mass elements[1] (which is in our case bone) within the sliding box of size r has to be counted (box mass s). This counting has to be repeated over the entire object producing the frequency distribution of the box masses $n(s, r)$.

A popular definition of the lacunarity uses the ratio of the second and first moment of this distribution $n(s, r)$ [14]:

$$\Lambda(r) = \frac{\mu_2(r)}{\mu_1^2(r)}, \tag{2.1}$$

where the first moment is

$$\mu_1(r) = \frac{1}{N} \sum_s s\, n(s, r), \tag{2.2}$$

the second is

$$\mu_2(r) = \frac{1}{N} \sum_s s^2\, n(s, r) \tag{2.3}$$

and N is the total number of boxes.

In a former definition of the lacunarity only the variance of the mass distribution was taken into account [6].

[1] This analysis can also be applied to non-binary data – if the total mass is spread evenly over the entire set, the lacunarity will be low, but if the mass is concentrated at a few points, however, lacunarity will be high.

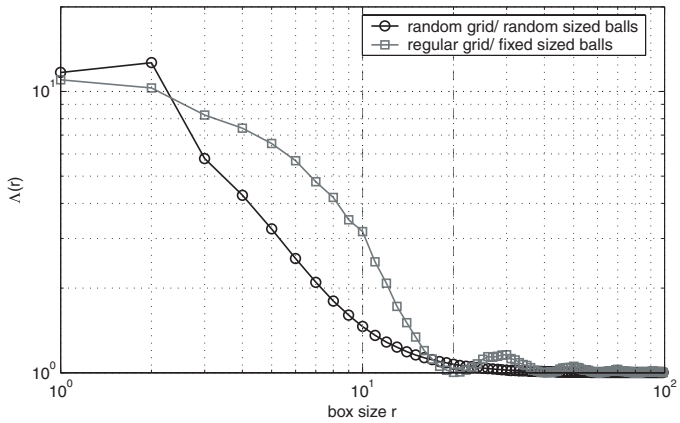

Fig. 2. Lacunarity for examples of random and regular distributed and sized objects.

This definition (2.1) of the lacunarity can be applied to one- and also to higher-dimensional data. The implementation for an analysis of 3D μCT images is straightforward.

Usually, this measure is computed as a function of box size r in an interval of $r \in [1, M/2]$ (where M is the size of the object) and plotted in a log-log plot (Fig. 2).

An alternative definition is the *normalized lacunarity* [5]

$$\Lambda^*(r) = 2 - \left(\frac{1}{\Lambda(r)} + \frac{1}{\overline{\Lambda}(r)} \right), \tag{2.4}$$

where $\overline{\Lambda}(r)$ is the complementary lacunarity (lacunarity of the complemented object), ensuring a lacunarity measure within the range 0 and 1.

From a log-log-plot of the lacunarity in respect to the box size r the following can be inferred:

1. **sparse patterns** have higher lacunarity than dense patterns for the same gliding box size;
2. $\lambda(r)$ **decreases for increasing** r, because larger boxes will be more translationally invariant than smaller boxes;
3. for a given object mass and box size higher lacunarity indicates greater clumping; if the box size reaches the size of the clumps, the curve declines more rapidly (**identification of scales**);
4. a linear decrease of the curve in the log-log plot reveals a large amount of **self-similarity** in the object.

In the following we illustrate the lacunarity measure with prototypical examples. We use two 3D objects, where the first consists of randomly distributed balls of random size and the second object consists of periodically distributed balls of fixed size $r = 10$ voxels (distance between the center of balls is 20 voxels).

The log-log plot of the lacunarity for the random object reveals a monotone increasing without any interesting changes in the slope (Fig. 2). The log-log plot for the regular object, however, reveals at the box size of $r = 10$ voxels a sudden change in the slope, which corresponds with the diameter of the balls. Where the box size reaches the period distance between the balls, the lacunarity becomes zero (at $r = 20$ voxels). The later periodic behaviour of the curve is due to the periodic arrangement of the balls.

In the log-log-plot of the normalized lacunarity for the same objects all the characteristic features which we have already found in the lacunarity plot are much more emphasized (Fig. 3). Using the normalized lacunarity it is easier to find the characteristic length scales for the regular object. The rather monotonic curve is typical for random objects without characteristic scales. Therefore, we focus on the normalized lacunarity henceforth.

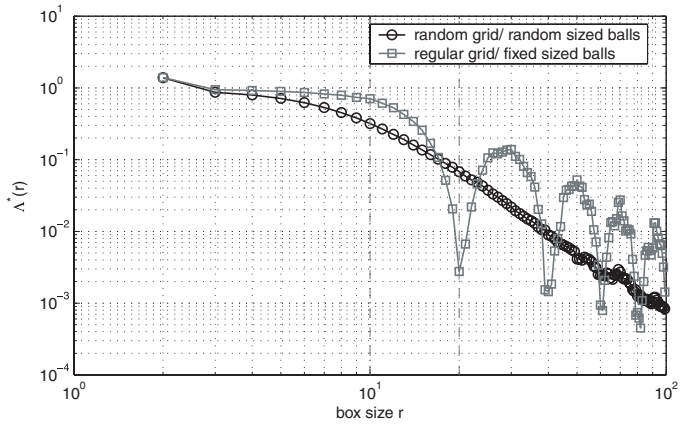

Fig. 3. Normalized lacunarity for examples of random and regular distributed and sized objects.

3 Moran's I index and geary's C index

Small-scale spatial auto-correlation can be quantified by using *Moran's I index* and *Geary's C index*. Originally from theoretical ecology, the Moran's I index has already found its way into 2D image analysis [1,3]. Here we will extend its definition properly in order to analyse 3D images.

The Moran's I index for a two-dimensional image is defined by [1,3]

$$I = \frac{N}{S_0} \frac{\sum_{j=1}^{d_1 \times d_2} \sum_{i=1}^{d_1 \times d_2} \delta_{ij} \left(x_i - \bar{x}\right) \left(x_j - \bar{x}\right)}{\sum_{i=1}^{d_1 \times d_2} \left(x_i - \bar{x}\right)^2}, \tag{3.1}$$

where d_1 and d_2 are the geometric size of the image (columns and rows), x_i is the value at the specified position, $\bar{x}$ is the mean of the image, $\delta_{ij} = 1$ if pixel i and j are adjacent and 0 otherwise, $N = d_1 d_2$ is the total number of pixels and $S_0 = \sum \sum \delta_{ij}$ is the number of contiguous pairs ($S_0 = 4d_1d_2 - 3(d_1 + d_2) + 2$; note that the equations for S_0 are not correct in the works of [1–3]). Its values varies between -1 and $+1$. If autocorrelation is high, the index will tend toward -1; if autocorrelation is high but negative, the index will tend toward $+1$ and if not correlated, the index will be zero.

For our purpose we have to extend the definition (3.1) to three dimensions:

$$I = \frac{N}{S_0} \frac{\sum_{j=1}^{d_1 \times d_2 \times d_3} \sum_{i=1}^{d_1 \times d_2 \times d_3} \delta_{ij} \left(x_i - \bar{x}\right) \left(x_j - \bar{x}\right)}{\sum_{i=1}^{d_1 \times d_2 \times d_3} \left(x_i - \bar{x}\right)^2}, \tag{3.2}$$

where S_0 is now

$$S_0 = 13 d_1 d_2 d_3 - 9 \left(d_1 d_2 + d_2 d_3 + d_3 d_1\right) + 6 \left(d_1 + d_2 + d_3\right) - 4. \tag{3.3}$$

Pairs of contiguous neighbours have to be counted only once. Therefore, the considered vicinity of a pixel is not a cube, but a more subtle geometric body (Fig. 4).

A similar measure as the Moran's I index is the *Geary's C index*, which is an average of the variation between adjacent pixels

$$C = \frac{(N-1)}{2S_0} \frac{\sum_{j=1}^{d_1 \times d_2 \times d_3} \sum_{i=1}^{d_1 \times d_2 \times d_3} \delta_{ij} \left(x_i - x_j\right)^2}{\sum_{i=1}^{d_1 \times d_2 \times d_3} \left(x_i - \bar{x}\right)^2}. \tag{3.4}$$

Values typically range between 0 and 2, where 0 indicates negative spatial autocorrelation, 2 indicates positive spatial autocorrelation and 1 no autocorrelation. This index is inversely

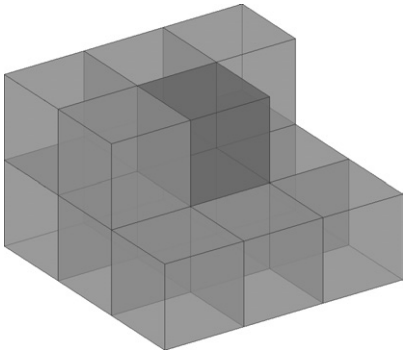

Fig. 4. Contiguous neighbours (gray) of a voxel (black) in 3D.

related to Moran's I index. However, Moran's I index gives a more global indicator, whereas Geary's C coefficient is more sensitive to differences in small neighbourhoods.

In the following we apply these indices to prototypical examples. We use three 3D objects, where the first consists of randomly distributed balls of random size, the second of periodically distributed plates of fixed size and the last of periodically distributed rods of fixed size. Plates and rods are typical micro-structures forming trabecular bone.

As expected, both measures are anti-correlated and regular structures are more anti-correlated than random structures (Fig. 5). The anti-correlation points to the fact that these measures quantify the interface between the rods/plates and the empty space around them. The change of the shape of the plates to, e.g., rods, changes the ratio between surface and volume of these micro-structures. This change of the shape is reflected by a change of the correlation. We find that rod-like structures are more anti-correlated than plate-like structures.

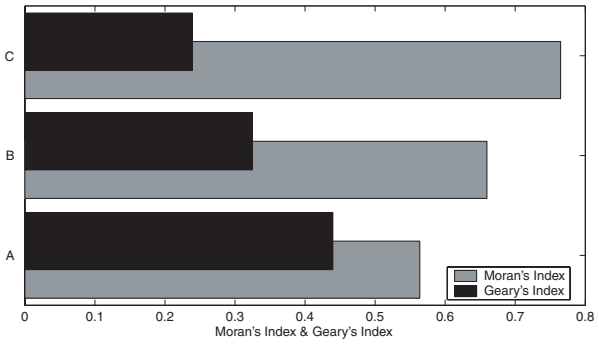

Fig. 5. Moran's and Geary's index for (A) random sized and distributed balls, (B) regularely distributed plates and (C) regularely distributed rods of fixed size.

4 Application to trabecular bone of proximal tibia

4.1 Materials

Now we apply the proposed measures to 3D μCT images of human proximal tibia. For this analysis, autopsy material comprising 16 women aged 57–92 years and 8 men aged 60–94 years is used [20]. None of these donators had any skeletal disease except some of the subjects had osteoporosis. Bone biopsies were taken 15 mm below the tibia plateau at the medial side, and have a cylindrical shape with a diameter of 7 mm and lengths of 20–40 mm. The biopsies were scanned with a *Scanco* μ *CT*40 scanner at Scanco Medical AG, Switzerland, using a voxel size of $20 \times 20 \times 20\,\mu\text{m}^3$.

The 24 μCT images are transformed to binary images by applying a threshold (1: bone; 0: marrow). The proposed measures are computed in a pre-defined volume of interest (VOI), which is a 10 mm long segment located 5 mm below the cortical bone [20].

4.2 Normalised lacunarity

The normalised lacunarity is computed using box sizes between 2 and 100 voxels (40–2000 μm). The sliding step is the same as the box size, i.e. the sliding box does not overlap.

At first we compare the normalised lacunarity Λ^* with the bone volume fraction BV/TV for a fixed box size of 20 voxels, i.e. 400 μm (Fig. 6). BV/TV is a measure with high correlation to bone strength and osteoporosis. The smaller BV/TV, the higher Λ^*, i. e. bone becomes more translational invariance during bone loss (development of osteoporosis).

The log-log-plots of Λ^* in regard of the box size r can be used to look on characteristic length scales (Fig. 7). The minima of the curves reveal characteristic lengths like sizes of trabeculae or distances between them. For the examples in Fig. 7 we find such minima at 1500 and 1750 μm for low BV/TV (0.11), at 1650 and 1780 μm for the examples with higher BV/TV (0.17 and 0.26). However, the biopsy with the highest BV/TV shows many minima which are not as clearly formed as in the other both examples with lower BV/TV. This is a sign of many different length scales in the trabecular bone, thus of a higher complexity of the trabecular bone structure.

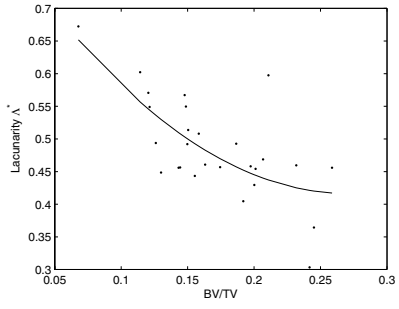

Fig. 6. Normalized lacunarity of proximal tibia for box size 400 μm.

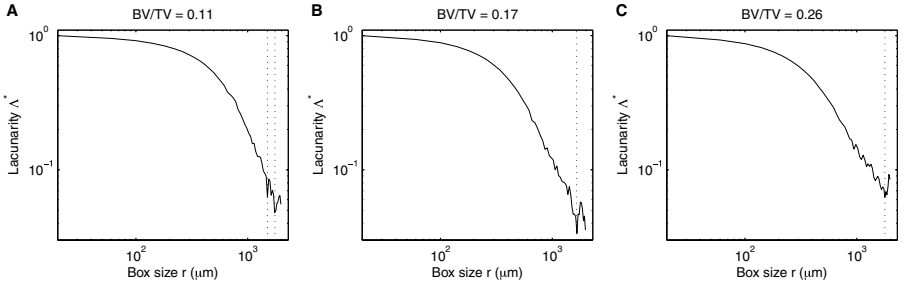

Fig. 7. Normalized lacunarity Λ^* as function of box size r for proximal tibia of three different bone volume fractions BV/TV: (A) 0.11, (B) 0.17 and (C) 0.26. The clear minima reveal characteristic length scales in the trabecular bone (see text for details).

From Fig. 3 we have learned, that the normalised lacunarity Λ^* for regularly distributed and sized structures exhibits a more sudden change of the slope. However, Λ^* decreases more slowly with increasing box size r for the irregular structures. For the three examples of trabecular bone, we find that the slope of Λ^* changes more slowly for higher BV/TV. From this finding we can again infer that the complexity of the bone is reduced during bone loss.

4.3 Moran's I and Geary's C index

Next we apply the Moran's I and Geary's C index to the μCT data of the proximal tibia biopsies. Both measures reveal high spatial anti-correlation with values between 0.79 and 0.87 (Moran's I) and between 0.15 and 0.25 (Geary's C). They exhibit a tendency of decreasing the spatial auto-(anti-)correlation for decreasing BV/TV (Fig. 8). This is a surprising result because it

could imply that the spatial structures become more randomly distributed and randomly sized for decreased BV/TV, i.e. bone loss (stronger osteoporosis). This is in contrast to the recent findings that the complexity would decrease with bone loss. On the other hand, both indices also distinguish between the shape of the trabeculae (cf. examples in Subsect. 3). Since we have found that the anti-correlation is higher in objects mainly consisting of rod-like structures than in objects consisting of plates, we can infer that the growth of the spatial anti-correlation during bone loss is caused by a change from mainly plate-like trabeculae to mainly rod-like trabeculae. This finding is confirmed by previous studies, where a change from plate-like to rod-like structures were found to be the main reason for bone loss during aging [24].

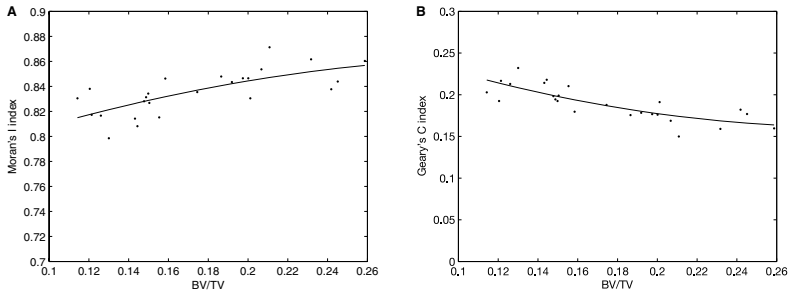

Fig. 8. (A) Moran's I and (B) Geary's C index for proximal tibia as functions of BV/TV.

5 Conclusion

In this study we have generalised measures of complexity based on fractal properties and spatial auto-correlation for the investigation of 3D images. The lacunarity measures translational invariance of 3D structures and can be used to detect characteristic length scales. Moran's I and Geary's C index measure spatial auto-correlation and are able to distinguish between different shapes of 3D micro-structures, like plates and rods.

Using lacunarity as well as Moran's I and Geary's C index, we have investigated trabecular bone of human proximal tibia, based on the analysis of 3D μCT images. We have found that the trabecular bone becomes more translational invariant and less complex during bone loss. The characteristic length scales of the trabeculae are also reduced during bone loss. Using Moran's I and Geary's C index we have found that the plate-like shape of trabeculae change to rod-like shapes during bone loss.

The proposed measures confirm previous findings of investigations using histomorphometry or structural measures of complexity. However, they used other properties of the trabecular bone. Moreover, the measures of complexity proposed here are quite simple to compute on the base of μCT images (in contrast to the invasive procedure of bone histomorphometry). They may be a good starting point for new quantitative descriptors of 3D structures, like trabecular bone.

This study was supported by grants from project MAP AO-99-030 (contract #14592) of the Microgravity Application Program/Biotechnology from the Human Spaceflight Program of the European Space Agency (ESA). The authors would also like to acknowledge Scanco Medical AG, Siemens AG, and Roche Pharmaceuticals for support of the study and thank Wolfgang Gowin and Erika May for preparation and scanning of the bone specimens.

References

1. T.-J. Chen, K.-S. Chuang, J. Wu, S.C. Chen, I.-M. Hwang, M.-L. Jan, Phys. Med. Biol. **48**, N131 (2003)
2. T.-J. Chen, K.-S. Chuang, J. Wu, S.C. Chen, I.-M. Hwang, M.-L. Jan, J. Digital Imag. **16**, 210 (2003)

3. K.-S. Chuang, H.K. Huang, Phys. Med. Biol. **37**, 357 (1992)
4. G. Delling, M. Amling, Nephrol. Dial. Transplant. **10**, 601 (1995)
5. G. Dougherty, G.M. Henebry, Med. Eng. Phys. **23**, 369 (2001)
6. Y. Gefen, A. Aharony, B.B. Mandelbrot, J. Phys. A **17**, 1277 (1984)
7. S.A. Goldstein, R. Goulet, D. McCubbrey, Calcified Tissue **53** (Suppl. 1); S127 (1993)
8. X.E. Guo, C.H. Kim, Bone **30**, 404 (2002)
9. T. Hildebrand, A. Laib, R. Müller, J. Dequeker, P. Rüegsegger, J. Bone Min. Res. **14**, 1167 (1999)
10. J.H. Kinney, J.S. Stölken, T.S. Smith, J.T. Ryaby, N.E. Lane, Bone **36**, 193 (2005)
11. B.B. Mandelbrot, *The fractal geometry of nature* (Freeman, San Francisco, 1982)
12. L. Mosekilde, A. Viidik, L. Mosekilde, Bone **6**, 291 (1985)
13. A.M. Parfitt, C.H.E. Mathews, A.R. Villanueva, M. Kleerekoper, B. Frame, D.S. Rao, J. Clin. Invest. **72**, 1396 (1983)
14. R.E. Plotnick, R.H. Gardner, W.W. Hargrove, K. Prestegaard, M. Perlmutter, Phys. Rev. E **53**, 5461 (1996)
15. L. Pothuaud, B. Van Rietbergen, L. Mosekilde, O. Beuf, P. Levitz, C.L. Benhamou, S. Majumdar, J. Biomech. **35**, 1091 (2002)
16. S. Prouteau, G. Ducher, P. Nanyan, G. Lemineur, L. Benhamou, D. Courteix, Eur. J. Clin. Invest. **34**, 137 (2004)
17. C.S. Rajapakse, J.S. Thomsen, J.S. Espinoza Ortiz, S.J. Wimalawansa, E.N. Ebbesen, L. Mosekilde, G.H. Gunaratne, J. Biomech. **37**, 1241 (2004)
18. J.-Y. Rho, L. Kuhn-Spearing, P. Zioupos, Med. Eng. Phys. **20**, 92 (1998)
19. P.I. Saparin, W. Gowin, J. Kurths, D. Felsenberg, Phys. Rev. E **58**, 6449 (1998)
20. P.I. Saparin, J.S. Thomsen, S. Prohaska, A. Zaikin, J. Kurths, H.-C. Hege, W. Gowin, Acta Astronaut. **56**, 820 (2005)
21. J.S. Thomsen, E.N. Ebbesen, L. Mosekilde, Bone **30**, 502 (2002)
22. B. van Rietbergen, S. Majumdar, W. Pistoia, D.C. Newitt, M. Kothari, A. Laib, P. Rüegsegger, Technol. Health Care **6**, 413 (1998)
23. L. Vico, P. Collet, A. Guignandon, M.-H. Lafage-Proust, T. Thomas, M. Rehailia, C. Alexandre, The Lancet **355**, 1607 (2000)
24. M. Vogel, M. Hahn, G. Delling, Bone **14**, 199 (1993)